



Publication Year	2019
Acceptance in OA@INAF	2021-01-21T11:31:29Z
Title	β UV slope of $z < 3$ bright ($L > L^*$) Lyman-break galaxies
Authors	Pilo, S.; CASTELLANO, MARCO; FONTANA, Adriano; GRAZIAN, Andrea; Boutsia, K.; et al.
DOI	10.1051/0004-6361/201834442
Handle	http://hdl.handle.net/20.500.12386/29914
Journal	ASTRONOMY & ASTROPHYSICS
Number	626

UV slope of $z \sim 3$ bright ($L > L^*$) Lyman-break galaxies in the COSMOS field

S. Pilo¹, M. Castellano¹, A. Fontana¹, A. Grazian¹, K. Boutsia², L. Pentericci¹, E. Giallongo¹, E. Merlin¹, D. Paris¹, and P. Santini¹

¹ INAF-Osservatorio Astronomico di Roma, Via Frascati 33, 00078 Monte Porzio Catone (RM), Italy
e-mail: stefano.pilo@inaf.it

² Carnegie Observatories, Las Campanas Observatory, Casilla 601, La Serena, Chile

Received 16 October 2018 / Accepted 23 January 2019

ABSTRACT

Context. The analysis of the UV slope β of Lyman-break galaxies (LBG) at different luminosities and redshifts is fundamental for understanding their physical properties, and in particular, their dust extinction.

Aims. We analyse a unique sample of 517 bright ($L > L^*$) LBGs at redshift $z \sim 3$ in order to characterise the distribution of their UV slopes β and infer their dust extinction under standard assumptions.

Methods. We exploited multi-band observations over 750 arcmin^2 of the COSMOS field that were acquired with three different ground-based facilities: the Large Binocular Camera (LBC) on the Large Binocular Telescope (LBT), the Suprime-Cam on the SUBARU telescope, and the VIRCAM on the VISTA telescope (ULTRAVISTA DR2). Our multi-band photometric catalogue is based on a new method that is designed to maximise the signal-to-noise ratio in the estimate of accurate galaxy colours from images with different point spread functions (PSF). We adopted an improved selection criterion based on deep Y -band data to isolate a sample of galaxies at $z \sim 3$ to minimise selection biases. We measured the UV slopes (β) of the objects in our sample and then recovered the intrinsic probability density function of β values (PDF(β)), taking into account the effect of observational uncertainties through detailed simulations.

Results. The galaxies in our sample are characterised by mildly red UV slopes with $\langle \beta \rangle \approx -1.70$ throughout the entire luminosity range that is probed by our data ($-24 \lesssim M_{1600} \lesssim -21$). The resulting dust-corrected star formation rate density (SFRD) is $\log(\text{SFRD}) \approx -1.6 M_{\odot} \text{ yr}^{-1} \text{ Mpc}^{-3}$, corresponding to a contribution of about 25% to the total SFRD at $z \sim 3$ under standard assumptions.

Conclusions. Ultra-bright LBGs at $z \sim 3$ match the known trends, with UV slopes being redder at decreasing redshifts, and brighter galaxies being more highly dust extinct and more frequently star-forming than fainter galaxies.

Key words. catalogs – galaxies: high-redshift – galaxies: evolution

1. Introduction

The introduction of the Lyman break technique more than 25 years ago (e.g. Steidel & Hamilton 1992, 1993) has enabled the selection of UV bright star-forming galaxies at $z \gtrsim 3$, thus opening a window on the earliest phases of galaxy formation at high redshift. Since then, the Lyman break method has been exploited to select objects at increasingly fainter magnitudes and higher redshifts, which extended our knowledge on the statistical properties of distant galaxy populations, such as the UV luminosity function (LF; e.g. Bouwens et al. 2015; Finkelstein et al. 2015; Ono et al. 2018; Oesch et al. 2018), the size distribution, and the size-luminosity relation (e.g. Grazian et al. 2012; Kawamata et al. 2015; Curtis-Lake et al. 2016).

Constraining the physical properties of Lyman-break galaxies (LBG) is fundamental for converting these global properties of the galaxy populations into global physical properties: most importantly, for inferring the total star-formation rate density (SFRD) from the UV LF. In practice, estimating the total SFRD requires knowing the conversion factor between the UV luminosity and the star formation rate (SFR), and of the amount of extincted UV radiation. The conversion between $L(\text{UV})$ and SFR has been routinely fixed on the basis of stellar population

synthesis models (e.g. Madau et al. 1998), while the slope β of the power-law UV continuum has acquired increasing importance for estimating dust extinction (e.g. Calzetti et al. 1994, 2000; Meurer et al. 1999). The UV slope is also affected by metallicity, age, star formation history, and stellar initial mass function, although dust extinction likely remains the dominant reddening factor (e.g. Wilkins et al. 2013; Castellano et al. 2014). While the conversion between observed luminosity and SFR is further complicated by uncertainties on the shape of the attenuation law of high-redshift galaxies (e.g. Capak et al. 2015; Reddy et al. 2018; McLure et al. 2018; Koprowski et al. 2018), accurate measurements of the UV slope of large samples of LBGs, and the determination of relations between UV slope, luminosity, and redshift, remain a fundamental ingredient for constraining the evolution of galaxies and the SFRD in the first ~ 2 Gyr after the Big Bang (Finkelstein et al. 2012; Bouwens et al. 2014). Unfortunately, discrepancies among different works remain on the β - $L(\text{UV})$ and β -redshift relations, which might be explained by differences in selection criteria and by a poor evaluation of the impact of observational effects and selection biases (e.g. Bouwens et al. 2009, 2012a; Castellano et al. 2012; Dunlop et al. 2013).

Table 1. Imaging dataset.

Filter	λ_{central} (nm)	Exp. time (s)	FWHM (arcsec)	AB Mag. limit ($S/N = 10$)	Instrument	Pixel scale ($\frac{\text{arcsec}}{\text{pixel}}$)
$U_{\text{special}}^{(a)}$	355	28 700	0.94	26.6 (26.8)	LBC (LBT)	0.225
$G_{\text{sloan}}^{(a)}$	475	12 200	1.12	27.1	LBC (LBT)	0.225
$R_{\text{sloan}}^{(a)}$	622	12 000	0.97	26.4	LBC (LBT)	0.225
$I_{\text{sloan}}^{(b)}$	764	27 000	0.97	25.8 (26.2)	Suprime-Cam (Subaru)	0.150
$Z_{\text{sloan}}^{(b)}$	903	38 880	1.15	24.9	Suprime-Cam (Subaru)	0.150
$Y^{(c)}$	1020	42 360	0.85	25.1 (26.0)	Vir-Cam (VISTA)	0.300
$J^{(c)}$	1250	49 720	0.81	24.9 (25.5)	Vir-Cam (VISTA)	0.300
$H^{(c)}$	1650	42 520	0.80	24.6 (25.0)	Vir-Cam (VISTA)	0.300
$K^{(c)}$	2150	39 400	0.80	24.1 (25.1)	Vir-Cam (VISTA)	0.300

Notes. The FWHM of the PSF has been measured on a stacking of a selected sample of bright non-saturated stars. Limiting magnitudes have been measured in diameter apertures of 2 arcsec. Because some images have variable depth across the field, we report in parentheses the limiting magnitude of the deepest portions in each band.

References. ^(a) Boutsia et al. (2014), ^(b) Taniguchi et al. (2007), and ^(c) McCracken et al. (2012).

In this paper we analyse the UV slope of a large sample of bright ($L \gtrsim L^*$) galaxies at $z \sim 3$, that is, at the peak of the SFRD. Compared to previous analyses of UV slopes at $z \sim 3$ (Bouwens et al. 2009; Finkelstein et al. 2012; Hathi et al. 2013; Kurczynski et al. 2014; Pannella et al. 2015), we exclusively focus on a large sample of galaxies in the high-luminosity range. In addition, we introduce new colour–colour criteria that combine optical and IR data and are aimed at an accurate and efficient selection of moderately extinguished LBGs. The determination of the UV slope distribution is carried out using the technique presented in Castellano et al. (2012; hereafter C12), which is meant to recover the intrinsic probability distribution function $\text{PDF}(\beta)$ taking into full account observational and selection effects. Particular care has also been taken in the construction of a multi-band photometric catalogue that maximises the accuracy of colours and UV slope measurements from imaging data at different resolution.

The structure of the paper is as follows: in Sect. 2 we present the dataset exploited in this paper; in Sect. 3 we describe the selection criterion we use for the extraction of the galaxy sample and assess its completeness and efficiency, and Sects. 4 and 5 present the results on $\text{PDF}(\beta)$ and SFRD measurements, respectively. Summary and conclusions (Sect. 6) follow. A detailed description of the new photometric method we used to extract the source catalogues is given in the appendix. Throughout the whole paper, observed and rest frame magnitudes are in the AB system, and we adopt the Λ -CDM concordance model ($H_0 = 70 \text{ km s}^{-1} \text{ Mpc}^{-1}$, $\Omega_M = 0.3$ and $\Omega_\Lambda = 0.7$).

2. Multi-band observations

We exploit imaging data in nine different bands over a common area of $\sim 750 \text{ arcmin}^2$ of the COSMOS field (Scoville et al. 2007). The dataset covers a spectral range from U band ($\lambda_{\text{central}} = 355 \text{ nm}$) to K band ($\lambda_{\text{central}} = 2150 \text{ nm}$), and it has been acquired by three different ground-based instruments. The U_{special} filter, the G -Sloan, and the R -Sloan_{blue} images were obtained with the Large Binocular Camera (Giallongo et al. 2008) at the LBT on Mount Graham in Arizona, and are described in Boutsia et al. (2014; see also Grazian et al. 2016, 2017). The I - and Z -band filter images (Taniguchi et al. 2007; Capak et al. 2007) have been acquired by the Suprime-Cam (Miyazaki et al. 2002) mounted on the Subaru Telescope at Maunakea. The J -, Y -, H -, and K -band images are from the second data release of the Ultra-VISTA survey (McCracken et al. 2012). The U , G , and R data

from LBC are significantly deeper than available Subaru data at similar wavelengths. In practice, we restrict our analysis to the portion of the full COSMOS area where deep LBC observations enable an accurate sampling of the Lyman break at $z \sim 3$. The main properties of our dataset are summarised in Table 1.

We used the LBC R band as detection image and extracted a multi-band photometric catalogue from all bands according to a new technique, which is described in detail in the Appendix. We used SExtractor (Bertin & Arnouts 1996) to measure the total (Kron) flux in the detection band, while total fluxes in the other bands were measured by scaling the total flux of the detection band according to the relevant colour terms. The novelty of our approach lies in the criteria we adopted to measure colours.

Briefly, we estimated the colour between the measure and detection images using optimally chosen apertures, scaled on the basis of the relevant PSF-FWHM in order to always recover the same fraction of flux in all bands for each source. This procedure allows the photometry to be extracted without resorting to PSF-matching techniques, thus preserving the original resolution in each image and avoiding any degradation of the photometric information. As shown in the appendix, the adopted technique enables colour (and UV slope) measurements at a signal-to-noise ratio (S/N) that is higher than can be achieved with PSF-matching techniques. The final catalogue includes 45 831 objects down to $R \sim 28$ (being $R = 26.4$ at $S/N = 10$, see Table 1).

3. $z \sim 3$ sample

3.1. New selection criterion for sampling U -dropout LBGs

We applied a tailored version of the Lyman-break technique (Steidel et al. 2003) to select LBGs at $z \sim 3$. The standard colour selection is based on a $(U - G)$ versus $(G - R)$ diagram (UGR criterion hereafter, e.g. Steidel & Hamilton 1992, 1993; Giavalisco 2002; Boutsia et al. 2014), where the U and G bands sample the 912 \AA break, and the $(G - R)$ colour samples the UV continuum of $z \sim 3$ star-forming galaxies. We used a different approach that takes advantage of the deep Y band instead of the R band. While selection criteria based on optical data alone, such as the UGR one, provide advantages in terms of observing efficiency and limiting depth, the availability of new, efficient IR detectors has enabled adopting IR colours in the selection of distant sources. It has indeed been shown (e.g. Beckwith et al. 2006; Castellano et al. 2012; hereafter C12) that exploiting

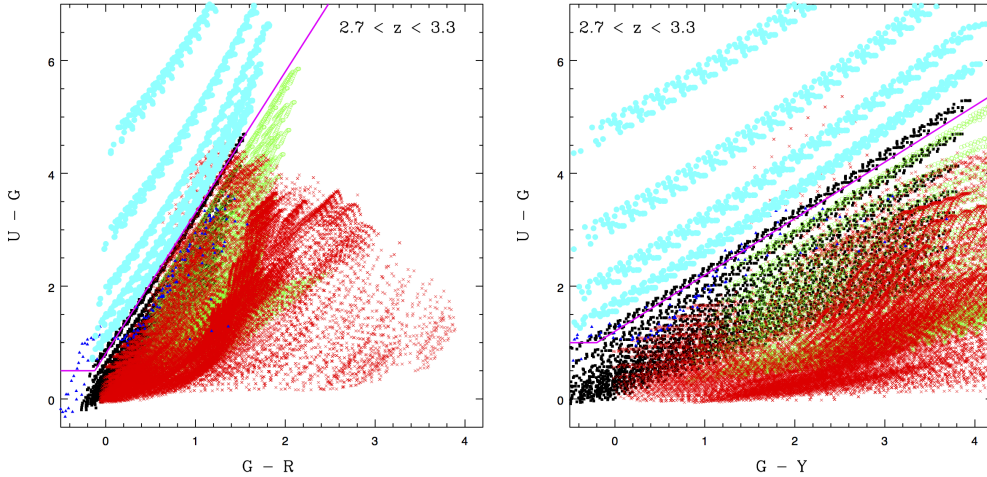


Fig. 1. Comparison between the *UGR* (left panel) and *UGY* criteria (right panel). Different colours and shapes mark the position of galaxy models. Cyan points mark the LBGs in the redshift range $2.7 < z < 3.3$ with $Z/Z_{\odot} = 0.2-1.0$, age = 0.01, 0.1, 0.3, 0.5, 1, 2 Gyr, constant SFR, at an increasing extinction $E(B-V) = 0-1.0$ at 0.05 intervals; black filled squares indicate LBGs out of the desired redshift range; red crosses indicate red passively evolving galaxies at lower redshifts, with $Z/Z_{\odot} = 0.2-1.0$, age = 1–13 Gyr, $\tau = 0.1, 0.3, 0.6$ at an increasing extinction $E(B-V) = 0-0.2$ at 0.05 intervals; green open circles mark low-redshift dusty star-forming galaxies with $Z/Z_{\odot} = 0.2-1.0$, age = 0.01–1 Gyr, constant SFH at an increasing extinction $E(B-V) = 0.5-1.5$ at 0.1 intervals; stars from the Pickles (1985) library are shown as blue filled triangles. The magenta continuous lines indicate the LBG selection windows.

a red filter improves the selection efficiency because it avoids contamination in the sample from dusty star-forming and passive galaxies at lower redshift.

Colour criteria were defined on the basis of models from Charlot and Bruzual 2007 (Bruzual 2007a,b; hereafter CB07) to efficiently separate LBGs from low-redshift interlopers:

$$U - G > 1.0 \wedge U - G > (G - Y) + 1.2.$$

These cuts were set after they were optimised on the basis of the analysis of spectroscopic redshifts in order to include as many sources as possible in the desired redshift range while avoiding the contamination of interlopers.

In Fig. 1 we compare the standard *UGR* selection criterion to the adopted *UGY* criterion, showing the positions of star-forming and passive galaxies with different ages, extinctions, metallicities, and with constant and also exponentially declining star formation histories (SFH). The *UGY* criterion clearly provides a clean selection of the LBGs in the target redshift range, regardless of their physical properties, and it enables the definition of conservative cuts to avoid contaminants. Low-redshift contaminants, especially red passive galaxies, are closer to moderate $E(B-V)$ LBGs in the *UGR* diagram than in the *UGY* diagram. A re-definition of the *UGR* selection window to make it more robust against photometric scatter appears unfeasible.

To avoid including objects with unreliable β values due to noisy photometry, we applied cuts at $R \leq 24.8$ and $Y \leq 25.3$, corresponding to an $R - Y = -0.5$ colour. This colour cut corresponds to $\beta \geq -3.0$, thus including all slope values that are predicted by standard stellar libraries. In practice, these criteria isolate objects with $S/N(R) \geq 20$ and with $S/N(Y) \geq 5 - 10$ in the shallower and in the deeper *Y*-band stripes, respectively. The observed *R* magnitude cut corresponds to a rest-frame cut at $M_{1600} \approx -20.8$.

This sample has been further refined by excluding

- sources that were identified as stars by visual inspection after checking all objects with SExtractor CLASS_STAR > 0.95,
- sources that were found to be X-ray emitters after cross-correlating our catalogue with McCracken et al. (2012) and Capak et al. (2007),

- objects that were not properly deblended, which have been detected as a unique source but at visual inspection were clearly found to be the blending of two distinct sources in at least one of the available bands,
- objects falling on artefacts, bad pixels, or at the very border of the image in at least one of the available bands, and
- objects falling into the halo of a nearby very bright saturated star in at least one of the available bands.

The final sample consists of 517 objects at $21.8 \leq R \leq 24.8$. The criteria described above ensure that our galaxy sample is not contaminated by stars, bright AGN (except any X-ray undetected AGN), or by spurious and problematic objects.

In Fig. 2 we show the relevant colour–colour diagrams and the differences between the criteria adopted in the present paper and the usual *UGR* selection. Our selected candidates are indicated by blue points, while the red points mark the position in the diagram of objects that would have been included by a standard *UGR* colour-selection, but are excluded from our sample.

We used the `zphot.exe` code with the well-tested procedure described in Fontana et al. (2000) and Grazian et al. (2006; see also Dahlen et al. 2013 and Santini et al. 2015) to compute photometric redshifts for our objects. We find an average $\langle z \rangle \approx 3.2$ for our LBG sample, in agreement with the expected redshift selection range.

3.2. Spectroscopic redshift validation of the sample

We cross-correlated our catalogue with the VUDS spectroscopic catalogue (Le Fèvre et al. 2014) and the DEIMOS 10 K Spectroscopic Survey Catalog of the COSMOS Field (Hasinger et al. 2018) to measure completeness in the target redshift range, and potential contamination by lower and higher redshift galaxy interlopers. We performed the cross-correlation in a 0.97 arcsec diameter corresponding to the *R*-band PSF-FWHM. We chose to take into account only sources with flags 3 and 4 (reliability $\geq 95\%$). We find that 54 sources in our *UGY* colour-selected sample ($\sim 11\%$) have a spectroscopic redshift: 42 objects ($\sim 80\%$) fall in the reference redshift range $2.7 < z < 3.3$ (the same as was used for evaluating the colour cuts from the libraries), 1 object

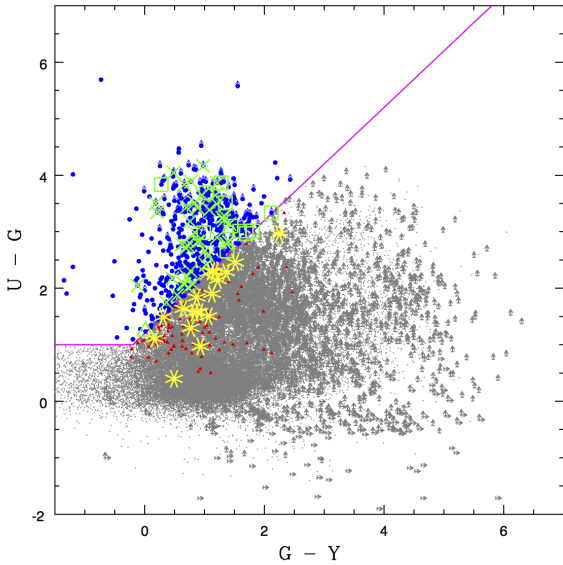


Fig. 2. *UGY* selected objects (blue points) along with objects selected with the *UGR* criterion that are excluded by the *UGY* criterion (red triangles). Upwards-pointing and right-pointing arrows mark upper limits in the *U* and *G* band, respectively. Objects with spectroscopic redshift in the range $2.7 < z < 3.3$ are marked as green crosses. Open triangles and open squares indicate sources at $z < 2.7$ and $z > 3.3$, respectively. Objects in the expected redshift range that are excluded by our selection are indicated in yellow.

(2%) is found to be at slightly lower redshift ($z = 2.68$), and 11 objects (18%) lie at $z = 3.32$ – 3.77 . No contamination from low-redshift interlopers is found, consistently with the expectation that the *UGY* criterion efficiently excludes red and dusty low-redshift galaxies. Seventeen sources at $2.7 < z < 3.3$ fall within our magnitude cuts but are not selected by our colour criteria: we find that all of them lie very close to the selection region in the colour–colour diagram and are excluded due to photometric scatter.

This scatter is inevitable when a pure colour selection criterion is applied because it stems from a combination of photometric noise and spectral variations of the sources. In Sect. 4.2 we describe how these observational uncertainties are fully taken into account in the estimate of UV slope distributions. In any case, we have verified that a modification of the colour cut in order to include these objects would worsen the contamination from low-redshift interlopers in the sample. We also verified that our *UGY* colour selection minimises this effect compared to the standard *UGR*. With this purpose, we repeated the same test using the standard *UGR* colour criterion. We find a lower selection efficiency with only 33 sources at $2.7 < z < 3.3$ included (together with 6 interlopers), and 26 sources excluded. We find that the *UGR* selection includes interlopers at a lower redshift ($z \sim 2.4$ – 2.5) than the *UGY* criterion. We conclude that the *UGY* selection is both more efficient and more robust than the standard *UGR* selection, at least at the depth of our dataset. Figure 2 shows the position of spectroscopic objects in our sample in the *UGY* colour–colour plane.

3.3. Selection completeness

We used Monte Carlo simulations to check the completeness of our sample as a function of β , which is measured from the *I*, *Z*, *Y* magnitudes as described in Sect. 4. We used CB07 libraries to produce a set of simulated galaxies in the redshift

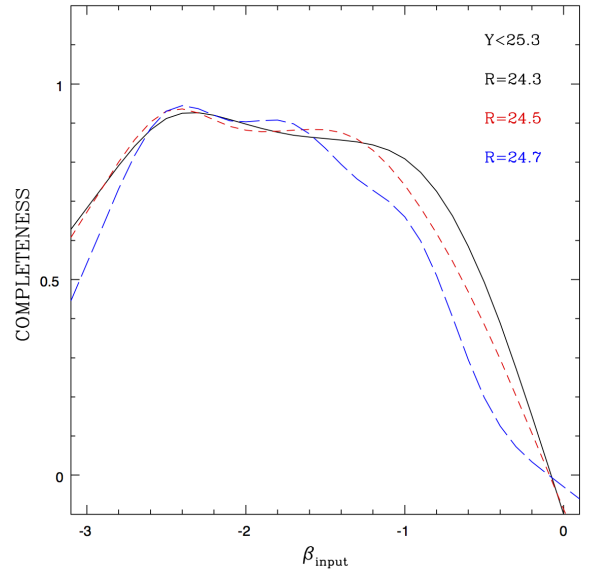


Fig. 3. Detection completeness as a function of β_{input} as found from our Monte Carlo simulations for sources with $Y < 25.3$ in magnitude bins centred at mag $R = 24.3, 24.5, 24.7$ (black continuous line, red short-dashed line, and blue long-dashed line, respectively).

range $2.5 < z < 3.5$. We considered galaxy models with constant SFHs and within the following range of physical parameters: $Z/Z_{\odot} = 0.02, 0.2, 1.0$, $0.01 \leq E(B-V) \leq 1.0$, $0.01 \leq \text{Age} \leq 1$ Gyr. We assumed a Salpeter (1955) initial mass function (IMF) and a Calzetti et al. (2000) attenuation law, while the transmission of the intergalactic medium (IGM) was treated according to Fan et al. (2006). We generated a mock catalogue of 5.6×10^5 objects by perturbing magnitudes in all the bands to match the relevant depths in the observed bands. The simulated catalogues were then treated and analysed like the real catalogues in order to evaluate the observational effects on galaxies of different magnitudes and spectral slopes. We evaluated the detection completeness of galaxies with a given input spectral slope β_{input} in different magnitude bins. Figure 3 shows that the applied cuts yield a completeness of $\sim 90\%$ at $-2.8 \leq \beta \leq -1.0$ (corresponding to $E(B-V) \leq 0.25$, following Calzetti et al. 2000) up to $R \approx 24.5$. The completeness at $R \approx 24.7$ decreases slightly more rapidly at red UV slopes but is still $\sim 70\%$ for $\beta \sim -1$. The 50% completeness limit lies at $\beta \sim -0.4$ – -0.8 ($E(B-V) \leq 0.30$ – 0.39) depending on the observed *R*-band magnitude. A similar test on a *UGR*-selected sample shows lower completeness levels for red objects, namely 50% completeness limits at $\beta \sim -0.7$ – -1.0 . In conclusion, we find that our selection criteria enable the analysis of a large range of physically meaningful values of β over the chosen range of magnitudes, and they improve the selection of red sources with respect to the standard *UGR* criteria.

4. UV slopes of $z \sim 3$ bright LBGs

4.1. Measurement of the UV slopes

We assumed the UV spectrum of the LBGs to be a power law $F_{\lambda} = \lambda^{\beta}$ and measured β by performing a linear fit over the observed *I*, *Z*, *Y* magnitudes (spanning the rest-frame wavelength range $\lambda \approx 1750$ – 2750 \AA at $z \sim 3$): $M_i = -2.5(\beta + 2.0) \log(\lambda_i) + c$, where M_i is the magnitude measured in the *i*th filter whose effective wavelength is λ_i . Uncertainties on the observed magnitudes were taken into account in deriving β and

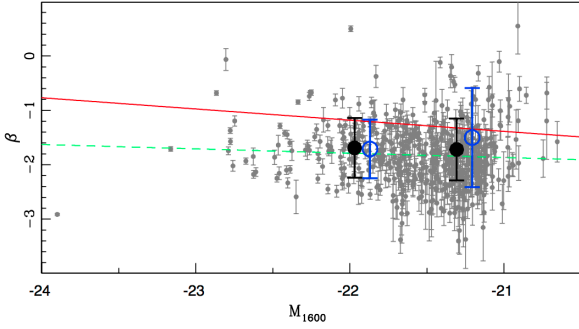


Fig. 4. UV slope as a function of M_{1600} . Black filled (blue open) circles show the best-fit values of the Gaussian (log-normal) distributions in each magnitude bin along with the relevant 1σ scatter. The mean β value is at $\langle\beta\rangle = -1.82$. The red line is the β -UV relation by Bouwens et al. (2009). The green dashed line marks the linear fit to our data.

its uncertainty, whose typical value is $\sigma_\beta \simeq 0.2$. We visually inspected a handful of objects (mostly with steep slopes) with larger errors (up to $\sigma_\beta \simeq 0.6\text{--}0.8$) to ensure that the larger uncertainty on β is due to a lower S/N rather than to systematics in their flux estimates.

The resulting observed relation between β and UV rest-frame magnitude at 1600 \AA is shown in Fig. 4. A linear fit on the observed relation is shown as the green dashed line in Fig. 4 and suggests little variation of the UV slope with luminosity: $\beta = (0.003 \pm 0.005) \cdot M_{1600} - 1.58 \pm 0.11$ (Spearman correlation coefficient $r_S = -0.09$). However, as discussed in C12 and highlighted in Sect. 3.3 of this paper, the observed magnitudes and colours affect the accuracy and completeness of UV slope estimates significantly. This implies that to measure the dependence of β on UV magnitude, and in particular to recover the probability distribution function of β at different luminosities, it is not sufficient to perform a straightforward fit to the observed distributions, but it is necessary to de-convolve such distributions from observational effects.

4.2. Recovering the intrinsic UV slope distributions

We followed the approach described in C12, which exploits Monte Carlo simulations to take into account all observational effects and any dependence of selection completeness on flux and colour in the estimate of the probability distribution function of the UV slopes, PDF(β).

In practice, (1) we assumed that the probability distribution function PDF(β) follows a given functional form, whose average ($\langle\beta\rangle$) and standard deviation ($\text{rms}(\beta)$) have to be estimated in different UV magnitude ranges. (2) For each ($\langle\beta\rangle$, $\text{rms}(\beta)$) pair in the parameter space of interest, we extracted a large number of galaxy templates at $2.5 < z < 4.0$ and randomly perturbed their fluxes, matching in each band the relevant relation between magnitude and S/N from our observed catalogue. (3) We applied our LBG selection criteria and measured the UV slope distribution of such a mock sample in the same way as for the real one. (4) We assessed the likelihood of each assumed pair of parameters by comparing the simulated and observed β distributions using a maximum likelihood estimator \mathcal{L} (e.g. Bouwens et al. 2008; Castellano et al. 2010a). Finally, the best-fit pair of parameters ($\langle\beta\rangle$, $\text{rms}(\beta)$) was found by minimising $\Delta\chi^2 = -2.0 \ln(\mathcal{L})$.

This procedure was separately applied to two different magnitude bins in order to obtain information on how the intrinsic PDF(β) varies with UV luminosity: the first bin is at $-24.0 < M_{UV} \leq -21.6$ (210 objects) and the second at

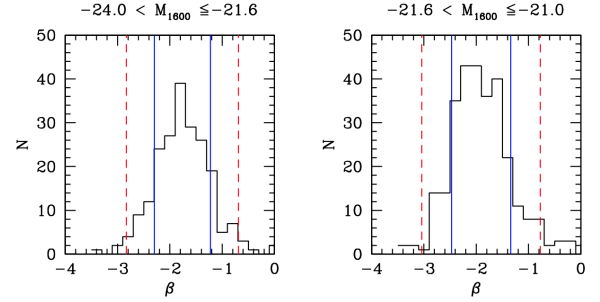


Fig. 5. Observed UV slope distributions at $-24.0 < M_{1600} \leq -21.6$ (left panel) and $-21.6 < M_{1600} \leq -21.0$ (right panel). The 1σ and 2σ dispersion ranges are included within the blue continuous and red dashed lines, respectively.

$-21.6 < M_{UV} \leq -21$ (288 objects). The choice of the bin widths is somewhat arbitrary, but ensures a suitable number of objects for the statistical analysis of each bin.

We assumed as the shape of the PDF(β) both a Gaussian (as has been suggested previously, e.g. Bouwens et al. 2009) and a log-normal distribution. As was noted by C12, the choice of a log-normal PDF(β) as alternative to a Gaussian is suggested by the shape of the observed UV slopes. As an example, the distribution in our faintest bin (right panel in Fig. 5) shows a tail of red objects, which suggests a possible asymmetric distribution with a bulk of low-extinction LBGs along with only few sources at higher $E(B - V)$ values.

Since the Monte Carlo simulations described in step (2) are time consuming, we first constrained the parameter space of interest by testing a wide range of ($\langle\beta\rangle$, $\text{rms}(\beta)$) values on a coarse sampling of the ranges $\langle\beta\rangle = -2.2, -1.0$ and $\text{rms}(\beta) = 0.1, 1.5$. We then accurately constrained their best-fit and confidence range through the analysis of a 35×35 grid in the range $\langle\beta\rangle = -2.0, -1.4$ for both the Gaussian and log-normal distributions, and $\text{rms}(\beta) = 0.4, 0.8$ (for the Gaussian distribution) and $\text{rms}(\beta) = 0.4, 1.0$ (log-normal). For each position in the grid and for each magnitude bin, we extracted 25 000 objects from the CB07 library and perturbed magnitudes in all bands as described in 3). We note that the estimate of \mathcal{L} in step (4) requires the observed and simulated UV slopes distributions to be binned: the choice of the bin widths was tailored to ensure that the extended but poorly populated tails in the observed distributions are efficiently sampled by the simulations. As shown in Fig. 5, different bin widths were thus set depending on the $1, 2, 3\sigma$ ranges of the observed distribution so as to reduce numerical noise in our procedure.

The best-fit parameters of the Gaussian and log-normal PDF(β) in each magnitude bin are reported in Table 2. Confidence regions for the PDF(β) are shown in Fig. 6, together with observed and best-fit distributions. It is also highlighted how the latter (blue lines) are reshaped by observational effects (red): only a full modelling approach such as presented in C12 and adopted in this work allows us to recover the intrinsic slope distributions from observations.

We find that $L > L^*$ objects at $z \sim 3$ have typical, average UV slopes ~ -1.7 . No significant variation with UV magnitude is found in the Gaussian case. The log-normal best-fit distributions point to a slightly redder average (~ -1.5) in the fainter bin, although with large correlated uncertainties between the parameters. The absence of a strong correlation between UV slope and magnitude is in agreement with what was found by C12 at $z \sim 4$, but it disagrees with the previous analysis of $z \sim 3$ objects by Bouwens et al. (2009).

Table 2. UV slope distribution: best-fit parameters and 68% c.l. uncertainties.

Gaussian			
UV magnitude	$\langle\beta\rangle$	rms(β)	
$M_{1600} \leq -21.6$	$-1.69^{+0.03}_{-0.07}$	$0.55^{+0.04}_{-0.07}$	
$-21.6 < M_{1600} \leq -21.0$	$-1.72^{+0.10}_{-0.09}$	$0.57^{+0.13}_{-0.06}$	
Log-normal			
UV magnitude	MAX	$\langle\beta\rangle$	rms(β)
$M_{1600} \leq -21.6$	$-1.98^{+0.05}_{-0.07}$	$-1.71^{+0.06}_{-0.08}$	$0.54^{+0.08}_{-0.07}$
$-21.6 < M_{1600} \leq -21.0$	$-2.07^{+0.18}_{-0.09}$	$-1.50^{+0.08}_{-0.09}$	$0.91^{+0.07}_{-0.13}$

While it is not possible to determine whether the best assumption is the Gaussian or the log-normal shapes, we note that the latter does not seem to accurately recover objects in the (poorly populated) left tail of the observed distribution in the brightest bin. This is also reflected in the noisier maximum likelihood contours.

4.3. Comparison with previous results

Investigations on the UV slopes of LBGs at similar redshifts and luminosities have been presented by Bouwens et al. (2009), Finkelstein et al. (2012), and Hathi et al. (2013), albeit on samples smaller than ours and using slightly different fitting techniques. We do not consider here the analysis by Kurczynski et al. (2014) and Pannella et al. (2015), which are mostly focused on fainter galaxies.

Bouwens et al. (2009) also suggested a Gaussian distribution and found a mean value $\langle\beta\rangle \simeq -1.18$ for a colour-selected sample of 168 bright LBGs ($\langle M_{UV} \rangle = -21.73$) at redshift $z \simeq 2.5$. Their mean UV slope is redder than our estimate, probably as a result of the lower redshift range probed and because they adopted different colour-selection criteria.

Finkelstein et al. (2012) exploited a sample of 177 galaxies selected on the basis of their photometric redshift and with $-22 \leq M_{1500} \leq -16$. Their sample has a mean photometric redshift of 3.42. They measured UV slopes on the best-fit templates of their objects and find a median β of $-1.82^{+0.00}_{-0.04}$ that shifts to $-1.80^{+0.03}_{-0.06}$ when the brightest galaxies of the sample are considered ($L > 0.75L^*$). These results are in agreement within the uncertainties with our findings in the same magnitude range (second magnitude bin in Table 2). Our redder mean value can be explained by the small difference in redshift between the two samples, or by the different methodologies adopted.

Hathi et al. (2013) analysed a sample of LBGs at $z \simeq 2.6$ and $z \simeq 3.8$, finding $\langle\beta\rangle = -1.71$ and $\langle\beta\rangle = -1.88$, respectively. They obtained these results by fitting a Gaussian to the observed β distribution to find the median value. At variance with our procedure, they did not take into full account the biases that are introduced by observational and selection effects. When we applied their simpler approach to our data, we find a mean $\langle\beta\rangle \sim -1.82$. This value falls in the middle of their estimates, in agreement with the well-established trend of decreasing typical β at increasing redshift.

We first compare in Fig. 7 our results to the estimates at $z \sim 3$ and to estimates at lower and higher redshifts in the same luminosity range from Bouwens et al. (2012b), Finkelstein et al. (2012), and C12. Our results properly fit in the well-established trend of decreasing UV slopes at increasing redshift and at fixed UV luminosity. In particular, a self-consistent comparison can

be made with the results by C12 at $z \sim 4$, where the very same method for recovering the intrinsic UV slope distributions was applied. The brightest galaxies in the C12 sample ($M_{UV} \lesssim -21$) have $\langle\beta\rangle = -1.90$, implying that in the ~ 500 Myr elapsed between redshift 4 and 3.2 the typical UV slopes increase by $\Delta\beta \simeq 0.2$, corresponding to an increase in extinction A_{1600} of $\simeq 0.4$ magnitudes assuming the insights of Meurer et al. (1999). Interestingly, there is a significant evolution in the scatter of the distribution that increases from $\text{rms}(\langle\beta\rangle) = 0.35$ at $z \sim 4$ to $\text{rms}(\langle\beta\rangle) = 0.56$ found in our sample. While an increase in dust extinction is the most likely explanation for this evolution, only a thorough investigation including a deep spectroscopic analysis (e.g. Castellano et al. 2014) can distinguish the contribution of dust and other factors (in particular, age and metallicity) to the observed trends. Moreover, this evolution between $z \sim 3$ and $z \sim 4$ seems to be stronger than the evolution suggested by measurements at other redshifts shown in Fig. 7.

The interpretation of the observed redshift- $\langle\beta\rangle$ trend at fixed luminosity is not straightforward because it may result from an evolution with redshift of the typical stellar mass of $L \sim L^*$ galaxies, given an underlying relation between stellar mass and dust extinction (Pannella et al. 2009, 2015; Reddy et al. 2010; Whitaker et al. 2014; Bouwens et al. 2016). We therefore compared our sample to similar samples that are available in the literature after estimating stellar masses of our objects through a spectral energy distribution (SED) fitting approach. We used the `zphot.exe` code and Bruzual & Charlot (2003) templates following the technique described in Castellano et al. (2014, 2016), finding masses in the range $\log(M_{\text{star}}/M_{\odot}) = 9-11$ and an average $\log(M_{\text{star}}/M_{\odot}) = 9.8 \pm 0.6$ (stellar IMF Salpeter 1955) for the galaxies in our sample. Our $\langle\beta\rangle \simeq -1.7$ is slightly redder than the extrapolation of the β -stellar mass at $z = 4$ presented by Finkelstein et al. (2012): they find an increasing slope at increasing stellar mass, with a median $\beta = -1.88$ at $z = 4$ and a nearly constant $\beta \sim -1.8$ at $z = 5-7$ for objects with $\log(M_{\text{star}}/M_{\odot}) = 9-10$. At $z \sim 2$, Reddy et al. (2018) found slopes that are redder than in our $z \sim 3$ sample: they measured $\langle\beta\rangle = -0.92(-1.88)$ for objects with masses higher (lower) than $\log(M_{\text{star}}/M_{\odot}) = 9.75$. We verified that our average $\langle\beta\rangle \sim -1.7$ does not significantly change when the sample is restricted to only the sources with $\log(M_{\text{star}}/M_{\odot}) > 9.75$. Overall, these results suggest that the relation between stellar mass and UV slope may experience a mild evolution up to $z \sim 3$ and a stronger one from $z \sim 3$ to ~ 2 . This trend is reminiscent of theoretical predictions on the mass-metallicity relation where a very mild evolution is found at $z \geq 3-4$ (Mittra et al. 2015; Davé et al. 2017). Assuming that a fixed fraction of metals are incorporated in dust, as suggested by observations at both low and high redshift (e.g. Draine et al. 2007; Chen et al. 2013), little evolution of the relation between mass and UV slope would be related to a mild increase at high redshift of the metallicity at fixed stellar mass.

5. Dust extinction and corrected SFR in bright $z \sim 3$ LBGs

5.1. Star-formation rate density of $L > L^*$ galaxies

The physical interpretation of our results is not straightforward because many factors affect the UV slope, although extinction is by far the main influencing factor (e.g. Wilkins et al. 2011). We can convert our β values into the average dust extinction at 1600 Å assuming standard relations. Following the widely adopted Meurer et al. (1999) relation, we find $A_{1600} \simeq 1.07$ ($A_{1600} \simeq 1.03$) and $A_{1600} \simeq 1.01$ ($A_{1600} \simeq 1.45$) for the

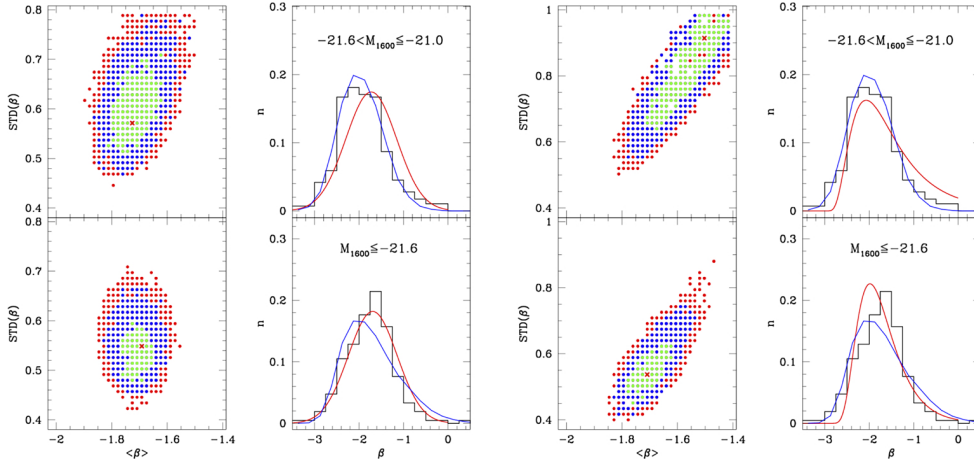


Fig. 6. Simulation results for the Gaussian (left panel) and log-normal (right panel) fit in the two different magnitude bins. In the leftmost column, we show maximum likelihood contours at 68%, 95%, and 99% c.i. in green, blue, and red, respectively; the red cross indicates the position of the best fit parameters. The rightmost column shows the histogram of the observed data and the relevant best-fit distribution. The red continuous line is the intrinsic $PDF(\beta)$, which is transformed into the blue continuous line by observational effects.

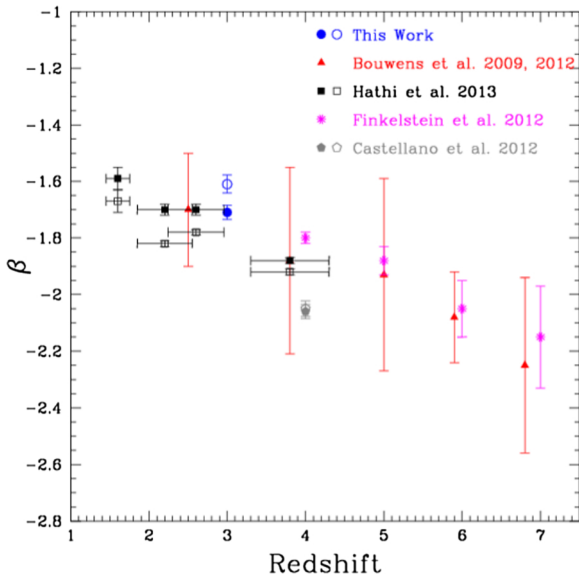


Fig. 7. Mean UV slope as a function of redshifts for $L \geq L^*$ galaxies from this work and from the literature. Estimates from Finkelstein et al. (2012) are for the $L > 0.75L^*$ range (Table 4 in their paper), while points from Bouwens et al. (2012b) are for objects with average $M_{UV} = -20.5$ up to $z = 6$, and $M_{UV} = -20.25$ at $z = 7$ (Table 4 in their paper). Filled and open symbols for this work and Castellano et al. (2012) indicate the Gaussian and the log-normal best-fit values, respectively. The median β values from Hathi et al. (2013) based on UV slope fits in the rest-frame 1300–1900 Å and 1300–3400 Å wavelength ranges are indicated as filled and open squares, respectively. Error bars for all the points indicate the 1σ uncertainty on the mean, except for the Bouwens et al. (2009, 2012b) $z = 4-5$ values, for which they are representative of the 1σ scatter.

Gaussian (log-normal) distribution in the bright and in the faint bin, respectively.

We can then evaluate the contribution from ultra-bright LBGs to the SFRD on the basis of the estimated $PDF(\beta)$ through the following equation:

$$SFRD = \frac{1.0}{8 \times 10^{27}} \int dL \int dA \cdot PDF(A, L) 10^{0.4A} \cdot L \cdot \Phi(L), \quad (1)$$

where the constant factor is from Madau et al. (1998), $A = A_{1600}$ such that $PDF(A, L)$ is univocally related to the $PDF(\beta, L)$ through the Meurer et al. (1999) relation, and $\Phi(L)$ is the UV luminosity function at 1600 Å (we adopt Schechter param-

eters from Reddy & Steidel 2009). The integral is evaluated separately for each of the two magnitude bins considering the relevant best-fit distribution $PDF(\beta)$, and the sum of the resulting values yields the SFRD at $L > L^*$ at $z = 3$. We obtain $\log(SFRD) = -1.63^{+0.21}_{-0.10} M_{\odot} \text{ yr}^{-1} \text{ Mpc}^{-3}$ for the Gaussian $PDF(\beta)$ and $\log(SFRD) = -1.57^{+0.06}_{-0.06} M_{\odot} \text{ yr}^{-1} \text{ Mpc}^{-3}$ for the log-normal PDF at $M_{UV} \leq -21.0$, which is the magnitude range probed by our data.

On the basis of the best-fitting SFRD function from Madau & Dickinson (2014) (Fig. 9 and Eq. (15)), $L > L^*$ LBGs contribute $\sim 25\%$ of the global value. This estimate is of course an upper limit if a non-negligible contribution to the SFRD at these redshifts came from optically undetected sub-millimeter galaxies (SMGs), such as those found by Santini et al. (2016) at $z \sim 3.3$ and Daddi et al. (2009) at $z \sim 4$.

Unfortunately, the A_{1600} and SFRD estimates strongly depend on assumptions on the attenuation curve and on the $A_{1600}-\beta$ relation. The latter depends on the intrinsic UV slope of the source, which in turn is determined by metallicity, age, SFH, and IMF of its stellar populations (e.g. Castellano et al. 2014; de Barros et al. 2014). We investigated how uncertainties in dust attenuation properties affect our SFRD estimate by adopting different attenuation curves and $A_{1600}-\beta$ conversion laws from the literature when we converted our $PDF(\beta, L)$ to the $PDF(A, L)$ used in Eq. (1). When we adopted the $A_{1600}-\beta$ relation by Castellano et al. (2014; Eq. (1) in their paper), which takes into account the low stellar metallicity measured in bright $z \sim 3$ LBGs (intrinsic UV slope $\beta_{\text{dust-free}} = -2.67$), we find a higher extinction ($A_{1600} \approx 1.93$ for the Gaussian distribution) resulting in an approximately twice higher SFRD ($\log(SFRD) = -1.28^{+0.11}_{-0.10} M_{\odot} \text{ yr}^{-1} \text{ Mpc}^{-3}$). The $A_{1600}-\beta$ relation from de Barros et al. (2014) (intrinsic UV slope $\beta_{\text{dust-free}} = -2.58$) yields $\log(SFRD) \approx -1.35 M_{\odot} \text{ yr}^{-1} \text{ Mpc}^{-3}$, which amounts to a 50% contribution to the global SFRD. A similar result is found with the best-fitting dust model estimated at $z \sim 5$ by Cullen et al. (2017). Similarly, SFRD estimates 25% higher than our reference value are found when the Gallerani et al. (2010) attenuation law is assumed, which is flatter than that of Calzetti et al. (2000), while the assumption of a Small Magellanic Cloud extinction leads to values 53% or 35% lower when the $A_{1600}-\beta$ conversions from Bouwens et al. (2016) and Reddy et al. (2018) are adopted, respectively. The results are summarised in Table 3. Uncertainties in the LF parameters also yield a comparable uncertainty on the SFRD: our estimates have to be revised upward by $\sim 30\%$ when the Schechter parameters from Cucciati et al. (2012) are adopted, while a $\sim 15\%$ increase is found when

Table 3. Contribution from $L > L^*$ galaxies to the SFRD at $z \sim 3$ under different assumptions.

$\log(\text{SFRD})$ $M_{\odot} \text{ yr}^{-1} \text{ Mpc}^{-3}$	Fraction	$A_{1600} - \beta$ conversion	Extinction law
$-1.63^{+0.21}_{-0.10}$	25%	Meurer et al. (1999)	Starburst ^(a)
$-1.28^{+0.11}_{-0.10}$	59%	Castellano et al. (2014)	Starburst ^(a)
$-1.35^{+0.10}_{-0.12}$	50%	de Barros et al. (2014)	Starburst ^(a)
$-1.33^{+0.10}_{-0.11}$	52%	Cullen et al. (2017)	Modified starburst ^(b)
$-1.53^{+0.12}_{-0.13}$	32%	Gallerani et al. (2010)	MEC ^(c)
$-1.96^{+0.04}_{-0.05}$	12%	Bouwens et al. (2016)	SMC ^(d)
$-1.82^{+0.05}_{-0.04}$	17%	Reddy et al. (2018)	SMC ^(d)

Notes. A Gaussian UV slope distribution and Schechter LF parameters from Reddy & Steidel (2009) are assumed in all cases. The reference total SFRD is taken from Madau & Dickinson (2014).

References. ^(a) Calzetti et al. (2000), ^(b) Cullen et al. (2017), ^(c) Gallerani et al. (2010), and ^(d) Gordon et al. (2003).

the LF from Mehta et al. (2017) or that from Viironen et al. (2018) is used.

5.2. UV slope as a function of dust-corrected UV luminosity

The usual analysis of trends between β and M_{UV} is mainly a useful tool to evaluate the correction to the observed UV luminosity functions and, eventually, to the SFRD (e.g. Dunlop 2013; Madau & Dickinson 2014, and references therein). However, it does not provide a clear mean to constrain the physical properties of the LBGs because dust affects both the UV slope and the observed UV magnitude. In order to evaluate the effect of dust as a function of an intrinsic galaxy property, we estimated the relation between β and the UV rest-frame magnitude corrected for the extinction $M_{1600\text{corr}} = M_{1600} - A_{1600}$. Figure 8 shows this relation along with a conversion of β and $M_{1600\text{corr}}$ into A_{1600} and SFR, respectively, estimated following Meurer et al. (1999) and Madau et al. (1998) (the adoption of different relations implies a rescaling of the units). Of course this conversion is still affected by a degeneracy, being A_{1600} estimated from β ; nevertheless it allows a direct visualization of how dust extinction evolves for galaxies at different luminosities. A clear trend seems to be in place, with extinction decreasing at increasing $M_{1600\text{corr}}$. The brightest galaxies are the dustiest and most star-forming, with $A_{1600} \gtrsim 2$, and $\text{SFR} \gtrsim 300 M_{\odot} \text{ yr}^{-1}$ at $M_{1600\text{corr}} \lesssim -24.5$. Our findings are in agreement with the analysis of the $M_{1600\text{corr}} - \beta$ relation at $z \sim 4$ presented in C12, and are consistent with a scenario where the more massive galaxies are more dust attenuated (e.g. Pannella et al. 2015; Bouwens et al. 2016).

6. Summary and conclusions

We have presented the analysis of the UV slopes of a large sample of bright $z \sim 3$ LBGs in the COSMOS field. We produced a photometric catalogue spanning the wavelength range from 335 nm to 2150 nm and exploited a new technique alternative to PSF-matching that maximises the S/N of colour measurements.

A selection criterion based on the U , G , and Y bands was used to select 517 $z \sim 3$ R -detected objects at $S/N(R) \geq 20$. The deep Y band enables a selection that is more efficient than can be achieved with the standard UGR criterion: in particular, a check on spectroscopically confirmed sources shows that our selection is characterized by a lower contamination from lower redshift interlopers and recovers more objects at $z \approx 2.7-3.3$. We measured the β slopes by performing a linear fit on the

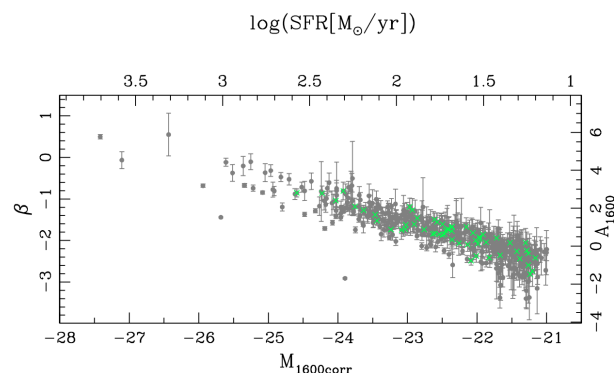


Fig. 8. UV slope as a function of dust-corrected UV magnitude. The figure also shows the conversion of these two quantities into extinction A_{1600} (Meurer et al. 1999) and $\log(\text{SFR})$ (Madau et al. 1998). Green crosses mark objects for which a spectroscopic redshift is available.

I , Z , Y magnitudes and evaluated observational uncertainties using extended simulations.

We carried out a parametric analysis of the UV slope distribution under the assumption that the intrinsic probability distribution function $\text{PDF}(\beta)$ is either Gaussian or log-normal. The best-fit values were found by comparing the observed and the simulated counts through a maximum likelihood estimator. We find a typical average $\langle \beta \rangle \approx -1.70$, with a dispersion $\text{rms}(\beta) \approx 0.55$. When comparing with the values measured at $z \sim 4$ with the same technique, we note a significant increase both in the average ($\langle \beta \rangle \approx -1.90$ at $z \sim 4$) and in the scatter of the distribution ($\text{rms}(\beta) \approx 0.35$ at $z \sim 4$). Our results fits well in the relation of β versus redshift, where galaxies are found to be bluer at increasing redshifts. The resulting contribution of ultra-bright LBGs to the $z \sim 3$ SFRD ($\log(\text{SFRD}) = -1.63^{+0.21}_{-0.10} M_{\odot} \text{ yr}^{-1} \text{ Mpc}^{-3}$ for the Gaussian $\text{PDF}(\beta)$) corresponds to $\sim 25\%$ of the global value. We also found a clear trend with decreasing extinction at increasing intrinsic UV magnitude.

Acknowledgements. We thank the anonymous referee for the useful suggestions and constructive comments that helped us to improve this paper. The research leading to these results has received funding from the European Union Seventh Framework Programme (FP7/2007–2013) under grant agreement No. 312725. The present work is based on observations carried out at the Large Binocular Telescope at Mt. Graham, AZ. The LBT is an international collaboration among institutions in the United States, Italy, and Germany. LBT Corporation partners are The University of Arizona on behalf of the Arizona university system; Istituto Nazionale di Astrofisica, Italy; LBT Beteiligungsgesellschaft,

Germany, representing the Max-Planck Society, the Astrophysical Institute Potsdam, and Heidelberg University; The Ohio State University; and The Research Corporation, on behalf of The University of Notre Dame, University of Minnesota, and University of Virginia.

References

- Beckwith, S. V. W., Stiavelli, M., Koekemoer, A. M., et al. 2006, *AJ*, **132**, 1729
- Bertin, E., & Arnouts, S. 1996, *A&AS*, **117**, 393
- Boutsia, K., Grazian, A., Giallongo, E., et al. 2014, *A&A*, **563**, A142
- Bouwens, R. J., Illingworth, G. D., Franx, M., & Ford, H. 2008, *ApJ*, **686**, 230
- Bouwens, R. J., Illingworth, G. D., Franx, M., et al. 2009, *ApJ*, **705**, 936
- Bouwens, R. J., Illingworth, G. D., Oesch, P. A., et al. 2012a, *ApJ*, **752**, L5
- Bouwens, R. J., Illingworth, G. D., Oesch, P. A., et al. 2012b, *ApJ*, **754**, 83
- Bouwens, R. J., Illingworth, G. D., Oesch, P. A., et al. 2014, *ApJ*, **793**, 115
- Bouwens, R. J., Illingworth, G. D., Oesch, P. A., et al. 2015, *ApJ*, **803**, 34
- Bouwens, R. J., Aravena, M., Decarli, R., et al. 2016, *ApJ*, **833**, 72
- Bruzual, A. G. 2007a, in *IAU Symp.*, A. Vazdekis, & R. Peletier, 241, 125
- Bruzual, G. 2007b, in *From Stars to Galaxies: Building the Pieces to Build Up the Universe*, eds. A. Vallenari, R. Tantaló, L. Portinari, & A. Moretti, *ASP Conf. Ser.*, **374**, 303
- Bruzual, G., & Charlot, S. 2003, *MNRAS*, **344**, 1000
- Calzetti, D., Kinney, A. L., & Storchi-Bergmann, T. 1994, *ApJ*, **429**, 582
- Calzetti, D., Armus, L., Bohlin, R. C., et al. 2000, *ApJ*, **533**, 682
- Capak, P., Aussel, H., Ajiki, M., et al. 2007, *ApJS*, **172**, 99
- Capak, P. L., Carilli, C., Jones, G., et al. 2015, *Nature*, **522**, 455
- Castellano, M., Fontana, A., Boutsia, K., et al. 2010a, *A&A*, **511**, A20
- Castellano, M., Fontana, A., Paris, D., et al. 2010b, *A&A*, **524**, A28
- Castellano, M., Fontana, A., Grazian, A., et al. 2012, *A&A*, **540**, A39
- Castellano, M., Sommariva, V., Fontana, A., et al. 2014, *A&A*, **566**, A19
- Castellano, M., Amorín, R., Merlin, E., et al. 2016, *A&A*, **590**, A31
- Chen, B., Dai, X., Kochanek, C. S., & Chartas, G. 2013, *ApJ*, submitted [arXiv:1306.0008]
- Cucciati, O., Tresse, L., Ilbert, O., et al. 2012, *A&A*, **539**, A31
- Cullen, F., McLure, R. J., Khochfar, S., Dunlop, J. S., & Dalla Vecchia, C. 2017, *MNRAS*, **470**, 3006
- Curtis-Lake, E., McLure, R. J., Dunlop, J. S., et al. 2016, *MNRAS*, **457**, 440
- Daddi, E., Dannerbauer, H., Stern, D., et al. 2009, *ApJ*, **694**, 1517
- Dahlen, T., Mobasher, B., Faber, S. M., et al. 2013, *ApJ*, **775**, 93
- Davé, R., Rafieferantsoa, M. H., Thompson, R. J., & Hopkins, P. F. 2017, *MNRAS*, **467**, 115
- de Barros, S., Schaerer, D., & Stark, D. P. 2014, *A&A*, **563**, A81
- Draine, B. T., Dale, D. A., Bendo, G., et al. 2007, *ApJ*, **663**, 866
- Dunlop, J. S. 2013, in *The First Galaxies*, eds. T. Wiklind, B. Mobasher, & V. Bromm, *Astrophys. Space Sci. Lib.*, **396**, 223
- Dunlop, J. S., Rogers, A. B., McLure, R. J., et al. 2013, *MNRAS*, **432**, 3520
- Fan, X., Strauss, M. A., Becker, R. H., et al. 2006, *AJ*, **132**, 117
- Finkelstein, S. L., Papovich, C., Salmon, B., et al. 2012, *ApJ*, **756**, 164
- Finkelstein, S. L., Ryan, Jr., R. E., Papovich, C., et al. 2015, *ApJ*, **810**, 71
- Fontana, A., D'Odorico, S., Poli, F., et al. 2000, *AJ*, **120**, 2206
- Galametz, A., Grazian, A., Fontana, A., et al. 2013, *ApJS*, **206**, 10
- Gallerani, S., Maiolino, R., Juárez, Y., et al. 2010, *A&A*, **523**, A85
- Giallongo, E., Ragazzoni, R., Grazian, A., et al. 2008, *A&A*, **482**, 349
- Giavalisco, M. 2002, *ARA&A*, **40**, 579
- Gordon, K. D., Clayton, G. C., Misselt, K. A., Landolt, A. U., & Wolff, M. J. 2003, *ApJ*, **594**, 279
- Grazian, A., Fontana, A., de Santis, C., et al. 2006, *A&A*, **449**, 951
- Grazian, A., Castellano, M., Fontana, A., et al. 2012, *A&A*, **547**, A51
- Grazian, A., Giallongo, E., Gerbasi, R., et al. 2016, *A&A*, **585**, A48
- Grazian, A., Giallongo, E., Paris, D., et al. 2017, *A&A*, **602**, A18
- Guo, Y., Ferguson, H. C., Giavalisco, M., et al. 2013, *ApJS*, **207**, 24
- Hasinger, G., Capak, P., Salvato, M., et al. 2018, *ApJ*, **858**, 77
- Hathi, N. P., Cohen, S. H., Ryan, Jr., R. E., et al. 2013, *ApJ*, **765**, 88
- Kawamata, R., Ishigaki, M., Shimasaku, K., Oguri, M., & Ouchi, M. 2015, *ApJ*, **804**, 103
- Koprowski, M. P., Coppin, K. E. K., Geach, J. E., et al. 2018, *MNRAS*, **479**, 4355
- Kurczynski, P., Gawiser, E., Rafelski, M., et al. 2014, *ApJ*, **793**, L5
- Le Fèvre, O., Amorin, R., Bardelli, S., et al. 2014, *The Messenger*, **155**, 37
- Madau, P., & Dickinson, M. 2014, *ARA&A*, **52**, 415
- Madau, P., Pozzetti, L., & Dickinson, M. 1998, *ApJ*, **498**, 106
- McCracken, H. J., Milvang-Jensen, B., Dunlop, J., et al. 2012, *A&A*, **544**, A156
- McLure, R. J., Dunlop, J. S., Cullen, F., et al. 2018, *MNRAS*, **476**, 3991
- Mehta, V., Scarlata, C., Rafelski, M., et al. 2017, *ApJ*, **838**, 29
- Merlin, E., Amorín, R., Castellano, M., et al. 2016, *A&A*, **590**, A30
- Merlin, E., Pilo, S., Fontana, A., et al. 2019, *A&A*, **622**, A169
- Meurer, G. R., Heckman, T. M., & Calzetti, D. 1999, *ApJ*, **521**, 64
- Mitra, S., Davé, R., & Finlator, K. 2015, *MNRAS*, **452**, 1184
- Miyazaki, S., Komiyama, Y., Sekiguchi, M., et al. 2002, *PASJ*, **54**, 833
- Oesch, P. A., Bouwens, R. J., Illingworth, G. D., Labbé, I., & Stefanon, M. 2018, *ApJ*, **855**, 105
- Ono, Y., Ouchi, M., Harikane, Y., et al. 2018, *PASJ*, **70**, S10
- Pannella, M., Carilli, C. L., Daddi, E., et al. 2009, *ApJ*, **698**, L116
- Pannella, M., Elbaz, D., Daddi, E., et al. 2015, *ApJ*, **807**, 141
- Pickles, A. J. 1985, *ApJS*, **59**, 33
- Reddy, N. A., & Steidel, C. C. 2009, *ApJ*, **692**, 778
- Reddy, N. A., Erb, D. K., Pettini, M., Steidel, C. C., & Shapley, A. E. 2010, *ApJ*, **712**, 1070
- Reddy, N. A., Oesch, P. A., Bouwens, R. J., et al. 2018, *ApJ*, **853**, 56
- Salpeter, E. E. 1955, *ApJ*, **121**, 161
- Santini, P., Ferguson, H. C., Fontana, A., et al. 2015, *ApJ*, **801**, 97
- Santini, P., Castellano, M., Fontana, A., et al. 2016, *A&A*, **596**, A75
- Scoville, N., Aussel, H., Brusa, M., et al. 2007, *ApJS*, **172**, 1
- Steidel, C., & Hamilton, H. 1992, *AJ*, **104**, 941
- Steidel, C., & Hamilton, H. 1993, *AJ*, **105**, 2017
- Steidel, C. C., Adelberger, K. L., Shapley, A. E., et al. 2003, *ApJ*, **592**, 728
- Taniguchi, Y., Scoville, N., Murayama, T., et al. 2007, *ApJS*, **172**, 9
- Viironen, K., López-Sanjuan, C., Hernández-Monteagudo, C., et al. 2018, *A&A*, **614**, A129
- Whitaker, K. E., Franx, M., Leja, J., et al. 2014, *ApJ*, **795**, 104
- Wilkins, S. M., Bunker, A. J., Stanway, E., Lorenzoni, S., & Caruana, J. 2011, *MNRAS*, **417**, 717
- Wilkins, S. M., Bunker, A., Coulton, W., et al. 2013, *MNRAS*, **430**, 2885
- Windhorst, R. A., Cohen, S. H., Hathi, N. P., et al. 2011, *ApJS*, **193**, 27

Appendix A: Photometric catalogue

A.1. New photometric method for estimating unbiased colours from images with different seeing

The images in our dataset have been acquired using different telescopes under a variety of observing conditions, which naturally leads to different point spread functions (PDFs). In this situation, the shape of a given object is smoothed in different ways in the various images, with the result that a standard fixed aperture photometry yields severely biased colours because apertures of the same size recover a different flux fraction in each image. The standard approach to deal with these inhomogeneous datasets is to match the PSFs through appropriate kernels (e.g. [Castellano et al. 2010b](#); [Galametz et al. 2013](#); [Guo et al. 2013](#); [Merlin et al. 2016](#)).

We present here a different method that does not imply the usual PSF-matching and thus avoids the loss of information arising from the degradation of higher resolution images to match lower resolution images. Our technique aims at defining apertures that enable a self-consistent flux measurement on images with different PSFs. It is of clear advantage in the analysis of UV slopes to achieve unbiased colour estimates at higher S/N than those of standard PSF-matched catalogues.

The first step is the definition for each image of an effective FWHM ($FWHM_{\text{eff}}$) enclosing a fixed fraction of the total flux of bright non-saturated stars, regardless of the exact shape of the PSF:

$$\frac{\text{FLUX_AUTO}}{\text{FLUX_APER}} = 1.5 \quad (\text{A.1})$$

where FLUX_AUTO is the Kron flux of the source ([Bertin & Arnouts 1996](#)) and FLUX_APER is the flux measured in a circular aperture with a diameter equal to $FWHM_{\text{eff}}$. The ratio was chosen as a trade-off between having enough flux at a reasonable S/N from very faint objects as well and avoiding too large and noisy apertures.

In practice, the $FWHM_{\text{eff}}$ value was found by successive approximations on each image of the dataset, and it is reported in Table A.1. The effective FWHM (which is different for each band) provides a reference unit that characterises the PSF in a given image.

The second step was to identify the optimum aperture in the detection image (R band in our case) that is designed to maximise the S/N of the photometric measurement for the objects of interest. Figure A.1 shows the S/N as a function of aperture diameter (in terms of times the $FWHM_{\text{eff}}$) for sources at different magnitudes (ranging from 22 to 26.5 mag at 0.5 mag intervals): the aperture maximising the S/N extends from $1 \times$ to $1.5 \times FWHM_{\text{eff}}$ at decreasing flux. Because the bulk of the sources in our sample has magnitude in the range $24.0 \lesssim R \lesssim 24.8$, we set the optimum aperture in this band to $1.25 \times FWHM_{\text{eff}}$.

The third and final step was the identification of matched apertures in the measurement images, that is, the apertures (in units of the relevant $FWHM_{\text{eff}}$) that enable measuring unbiased colours on all sources of interest. This was done through intensive image simulations based on the H_{160} image from the GOODS-ERS WFC3/IR dataset (HST Programme ID 11359, [Windhorst et al. 2011](#)), which has a uniform depth and PSF ($FWHM_{H_{160}} = 0.18$ arcsec) across ~ 45 arcmin². By smoothing this image with appropriate convolution kernels, we obtained from it images with a seeing that ranged from 0.6 arcsec to 1.2 arcsec at 0.1 arcsec intervals. Clearly, all objects are expected to have a colour term equal to zero in all images in this dataset.

Table A.1. $FWHM_{\text{eff}}$ of the images.

Filter	$FWHM_{\text{eff}}$ (arcsec)
U_{special}	1.37
G_{sloan}	1.80
R_{sloan}	1.43
I_{sloan}	1.28
Z_{sloan}	1.59
Y	1.67
J	1.48
H	1.34
K	1.13

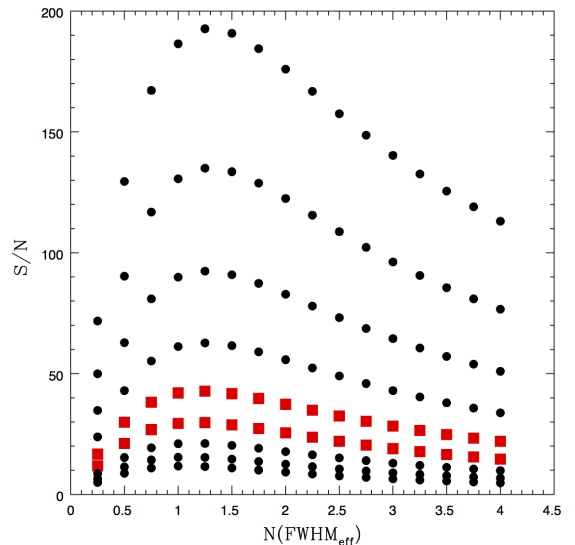


Fig. A.1. Mean R -band S/N in different photometric apertures defined in terms of the $FWHM_{\text{eff}}$, for objects in nine different magnitude bins at $22.0 \lesssim R \lesssim 26.5$ (from top to bottom). The $24.0 \lesssim R \lesssim 24.5$ and the $24.5 \lesssim R \lesssim 25.0$ bins where the bulk of our sources are found are shown as red filled squares.

We then ran SExtractor on dual-image mode on all images and searched for the apertures that yielded the expected colours. We found the following empirical relation between the size of the optimal aperture ($A_{\text{per, meas}}$) and the $FWHM_{\text{eff}}$ of the detection and measurement images:

$$A_{\text{per, meas}} = 0.4 \times [FWHM_{\text{eff}}(\text{det}) - FWHM_{\text{eff}}(\text{meas})] + 1.25. \quad (\text{A.2})$$

Figure A.2 shows the relation in Eq. (A.2): the red line represents a linear fit to the data with slope and intercept equal to 0.4 and 1.26, respectively.

A.2. Multi-band catalogue for the COSMOS dataset

The procedure described above was used in the analysis of our COSMOS dataset. We used the R -band mosaic as detection image and ran SExtractor in dual-image mode to measure the magnitudes in all bands. The magnitude of the sources in each band was set to

$$\text{mag}_{\text{filter}} = R_{\text{TOT}} + (\text{mag}_{\text{aper, filter}} - \text{mag}_{\text{aper, R}}), \quad (\text{A.3})$$

where total magnitudes in the R band were computed using SExtractor MAG_AUTO, and apertures were defined following Eqs. (A.1) and (A.2).

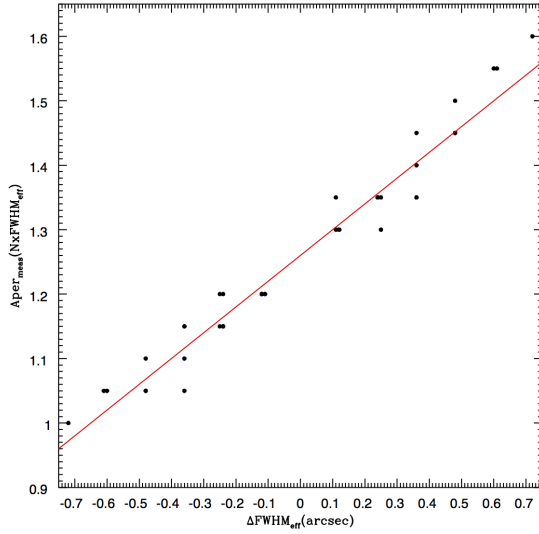


Fig. A.2. Empirical relation (A.2). Black dots show the size of the photometric aperture in units of $FWHM_{\text{eff}}$ of the measurement image. The red line shows the linear fit to the data.

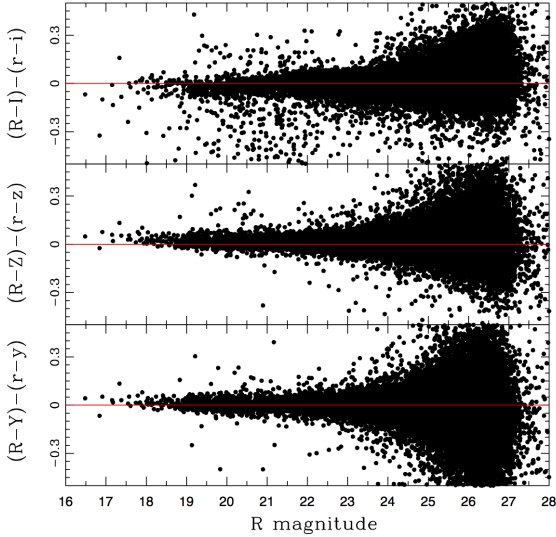


Fig. A.3. Comparison between colours from our catalogue and those from a catalogue built using the standard PSF-matching procedure. Capital letters are used for the magnitudes in our catalogue, and lower case letters indicate the magnitudes in the PSF-matched catalogue. The bulk of bright outliers at $R \sim 19\text{--}23$ in the *top panel* are found to be saturated stars in the *I*-band image.

We tested our procedure by comparing the resulting catalogue to an *R*-detected catalogue extracted following the standard PSF-matching approach. In the latter case, total magnitudes are extracted following Eq. (A.3), where the colour term was instead evaluated between images smoothed to the *Z*-band PSF, which is the coarser in the dataset. We checked the accuracy of the PSF-matching procedure by measuring the PSF growth curve for each smoothed image. We found that the matching is accurate to within 3% at twice the FWHM, which is the fixed size within which we measure colours in this case. Figure A.3 shows a comparison between the colours evaluated with the two different methods. Only colours between bands that are involved in the measurement of β are shown; all other combinations were tested as well and show similar results.

In order to quantify possible biases introduced by our technique in the measurement of β , we re-estimated UV slopes for all

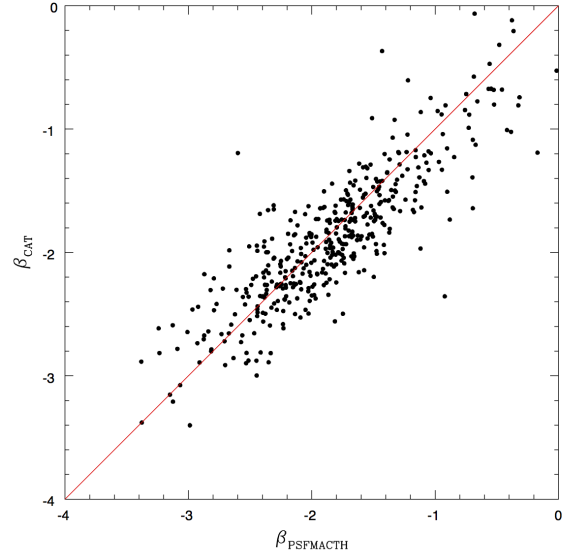


Fig. A.4. Comparison between UV slopes from our catalogue and those from a catalogue built using the standard PSF-matching procedure. The red line marks the equality relation.

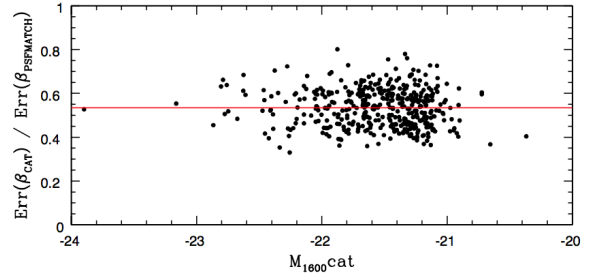


Fig. A.5. Ratio between the uncertainty on UV slope measured from our reference catalogue and from the PSF-matched catalogue as a function of UV rest-frame magnitude of the sources. The red line at 0.53 marks the average value of the ratio.

objects in our sample using magnitudes from the PSF-matched catalogue. We find an average $\langle \beta_{\text{PSFMATCH}} \rangle = -1.81 \pm 0.03$, perfectly consistent with the $\langle \beta \rangle = -1.82 \pm 0.03$ found in our reference catalogue. In Fig. A.4 we show a comparison between the two UV slope estimates for all objects.

All these tests show no evident systematics between our photometric method and the standard PSF-matching procedure. Small differences in photometry on single sources are most likely due to

- imperfections in the PSF extraction or in the creation of the PSF-matching kernels
- the uncertainty in the evaluation of $FWHM_{\text{eff}}$ on which our photometric technique is based.

These issues are under investigation and will be further improved. In particular, our technique can be improved by adopting elliptical apertures that will allow us to better follow the galaxy profiles, and by an automatic search of apertures that maximise the S/N (e.g. APHOT, Merlin et al. 2019).

Finally, we compared the uncertainty on β between the two different approaches object by object. Figure A.5 shows that errors on the UV slopes measured from our catalogue are lower by a factor of ~ 2 (on average) than in the case when the PSF-matched catalogue is used. This shows that our approach enables measuring β at a higher S/N than when previous photometric procedures are adopted.